Study of the Eutectoid Transformation in Nodular Cast Irons in Relation to Solidification Microsegregation

ALEXANDRE FREULON, PHILIPPE DE PARSEVAL, CLAUDIE JOSSE, JACQUES BOURDIE, and JACQUES LACAZE

Eutectoid transformation in cast irons may proceed in the stable or the metastable systems giving ferrite and graphite for the former and pearlite for the latter. The present work demonstrates that composition profiles across ferrite/pearlite boundaries are smooth and similar to those issued from the solidification step. No trace of long-range diffusion of substitutional solutes due to austenite decomposition could be observed. In turn, this ascertains that both stable and metastable transformations proceed with the product matrix—either ferrite or pearlite—inheriting the parent austenite content in substitutional solutes. This result sustains a physical model for eutectoid transformation based on the so-called local para-equilibrium which is commonly used for describing solid-state transformation in steels.

I. INTRODUCTION

THE final matrix of common nodular cast irons results from the eutectoid decomposition of high-temperature austenite and consists in either ferrite, pearlite, or a mixture of ferrite and pearlite. The former eutectoid transformation proceeds in the stable system (austenite → ferrite + graphite), the latter in the metastable system (austenite → ferrite + cementite). In practice, a low cooling rate is used during the eutectoid reaction in order to ensure a fully ferritic matrix. On the opposite, pearlite promoter elements such as Cu, Mn, Sb, or Sn are added to cast iron alloys for getting a fully pearlitic matrix even at quite low cooling rate.

Mastering of cooling conditions and alloy composition for obtaining a desired microstructure is made complicated because of chemical heterogeneities build-up during solidification, the so-called microsegregations. Heterogeneities in carbon are easily handled because this element diffuses quite fast in austenite. On the contrary homogenization of all elements but C and N cannot be carried out by any practical means, so that the eutectoid transformation takes place locally under

ALEXANDRE FREULON, Technician, and JACQUES LACAZE, Senior Scientist, are with CIRIMAT, Université de Toulouse, ENSIACET, CS 44362, 31030 Toulouse, France. Contact e-mail: Jacques.lacaze@ensiacet.fr PHILIPPE DE PARSEVAL, Research Engineer, is with GET, UMR 5563 CNRS, Université de Toulouse, 14 Avenue Edouard Belin, 31400 Toulouse, France, and also with the Centre de Microcaractérisation Raimond Castaing, Université de Toulouse, UMS 3623, 3 rue Caroline Aigle, 31400 Toulouse, France. CLAUDIE JOSSE, Engineer, is with the Centre de Microcaractérisation Raimond Castaing, Université de Toulouse, France. JACQUES BOURDIE, Ph.D. Student, is with CIRIMAT, Université de Toulouse, and also with Saint-Gobain Pont-à-Mousson, 21 avenue C. Cavallier, 54700 Pont-à-Mousson, France.

conditions that change at the microstructure scale.[1–3] The first aim of this work was to characterize the distribution of the elements at the local scale and to investigate if the eutectoid transformation may have affected the distribution issued from solidification.

Very little of tin or antimony, meaning less than 0.1 mass pct, is effective in decreasing the amount of ferrite, when 0.5 to 1.0 mass pct of copper and/or manganese is necessary to significantly decrease it. This suggests that the pearlite promoter effect of these various elements proceeds by different mechanisms. While a mechanism has been proposed for explaining the role of copper and manganese,[4] it has been observed that tin proceeds in a different way[5] and it is suspected that antimony affects the eutectoid transformation as tin does. The present work was also carried out to look for similarities with tin in case of low antimony addition.

In the present study a common nodular cast iron without and with a small addition of antimony was prepared and cast in blocks. The as-cast microstructure clearly showed the effect of antimony and this suggested using differential thermal analysis (DTA) to record eutectoid transformation temperatures during cooling at various rates after reaustenitization. As-cast samples and DTA samples were then investigated with optical microscopy (OM), focused ion beam (FIB) coupled with energy dispersive analysis (EDS), and electron microprobe.

II. EXPERIMENTAL DETAILS

The two alloys considered in this study were obtained from the same base melt, with the second one modified with a small addition of antimony (the target was 0.01 mass pct Sb). The first alloy will be called reference alloy in the following, the second one Sb-bearing alloy. The

melt was prepared in a 250 kg induction furnace with pig iron for the charge and addition of ferro-silicon alloy (Fe75Si) for adjusting the silicon content. After super-heating to 1773 K (1500 °C), the melt was poured in a 30 kg capacity transfer ladle at the bottom of which the nodulizing alloy had been placed covered with steel scrap. This nodulizing alloy was an FeSiMg alloy containing 8 mass pct Mg and added in an amount of 1.3 pct of the melt weight. Antimony addition was also achieved by depositing pure Sb at the bottom of the transfer ladle together with the nodulizing alloy. The melt was then poured in 2.5 kg blocks (40 × 50 × 175 mm³). Inoculation was achieved by adding 0.2 pct of the melt weight of a commercial inoculant at the bottom of each block and a thermocouple was placed into the mold in order to record the temperature evolution during solidification and cooling. The solidification time was in the range of 2 minutes and the cooling rate just before the eutectoid transformation about 7 K/min.

Carbon and sulfur were analyzed by combustion on a medal taken from the base melt. Other analyses were carried out on samples taken from the cast blocks. Silicon was quantified by gravimetric method and all other elements considered were analyzed by inductive coupled plasma spectroscopy after acid dissolution. The compositions of the two alloys are listed in Tables I and II, respectively. The content in Ba, Ce, and La was also measured and found lower than the detection limit at 0.0005 mass pct for all three elements.

DTA experiments have been performed using a Setsys 16/18 Setaram apparatus on small cylindrical samples (3.8 mm in diameter, 5 mm in height) machined out from the blocks. The samples were heated to 1223 K (950 °C), held at that temperature for carbon homogenization, then cooled to 873 K (600 °C) and reheated again to 1223 K (950 °C), and finally cooled down to room temperature. All heating sequences were performed at 20 K/min while various rates were used for cooling: in the so-called "short" cycle, the cooling rate was successively 20 and 5 K/min while in the "long" cycle they were 10 and 2 K/min. A new sample was used for each cycle, which means that two DTA samples were available for each alloy.

One sample from each block and the four DTA samples were then prepared by standard metallographic techniques for further investigation by optical microscopy, focused ion beam, and microprobe analysis.

Cross section of the as-cast samples have been obtained by FIB, on a FEG-SEM/FIB FEI HELIOS 600i coupled with an EDX Oxford Instruments analyzer Aztec Advanced equipped with an SDD detector. The sample was tilted (52 deg) towards the FIB column such that the ion beam was normally incident on the sample surface. The region to be analyzed was first protected by a Pt deposit, then a hole was milled in front of it creating a flat surface perpendicular to sample surface. A high Ga^+ ion beam current was initially used to rapidly mill the area to a depth of 20 to 50 μm, and then a finer beam with a much smaller beam current was applied to polish one face of the cross section. The polished face was imaged directly with the scanning electron microscope (SEM) and its composition analyzed by EDS with a 10 keV accelerating voltage. These chemical analyses are only qualitative because of the sample tilt.

Microprobe analyses were carried on all six samples. After metallographic preparation, these samples were etched and micro-hardness marks were made so as to easily locate appropriate areas afterwards. The samples were then slightly polished to remove etching marks and introduced into the microprobe. Quantitative analyses were performed using a Cameca SX Five with the following operating conditions: accelerating voltage 15 kV; beam current 50 nA; counting time on peak of 20 seconds for Al Kα, Mg Kα, Si Kα, Mn Kα and Cu Kα, 30 seconds for Cr Kα and P Kα, and 60 seconds for Sb Lα. The background was measured on both sides of every peak during a time half of that used for the peak. The following standards were used: periclase (MgO), corundum (Al_2O_3), wollastonite ($SiCaO_3$), pyrophanite ($MnTiO_3$), and pure metals for Cr, Cu, and Sb. After measurements, the apparent contents were corrected with the software PeakSight 5.1 to account for

Table I.   Composition (Mass Pct) of the Reference Alloy

C	Si	Mg	Mn	Ti	Al	Sb	S
3.80	1.91	0.025	0.198	0.031	0.012	0.0006	0.014

V	Cr	Mo	Ni	Cu	Ca	P	Fe
0.007	0.035	0.008	0.032	0.052	0.0025	0.061	balance

Table II.   Composition (Mass Pct) of the Sb-Bearing Alloy

C	Si	Mg	Mn	Ti	Al	Sb	S
3.80	2.10	0.025	0.186	0.027	0.015	0.0087	0.014

V	Cr	Mo	Ni	Cu	Ca	P	Fe
0.007	0.032	0.007	0.030	0.053	0.0024	0.059	balance

absorption and fluorescence. In this step, Fe was calculated by difference to 100 pct, which may lead to slight biases as carbon was not accounted for. For all analyzed elements and every measurement, the software indicates the detection limit and the standard deviation σ.

Microprobe measurements were realized in the spot mode along lines selected on the basis of the OM microstructure observations. According to the conditions used for analysis, the beam has a diameter slightly lower than 2 μm at the surface of the sample. Each spot lets a mark where the beam hits the sample that is due to cracking of residual gas by the accelerated electrons. Lines of analysis points may then be easily located by OM microscopy and have been photographed. When needed, a new etching was performed to ensure where the microprobe lines went through. On the whole, 21 microprobe lines were realized in about 30 hours. The settings of the microprobe were checked regularly during this time.

III. RESULTS

Figure 1 compares the as-cast microstructure of the reference and Sb-bearing alloys after Nital etching. The graphite nodules in dark contrast are well formed and encapsulated in ferrite that appears in light contrast, while the remaining of the matrix in gray contrast is pearlite. It is seen that a much larger amount of pearlite is present in the Sb-bearing alloy than in the reference alloy.

Figure 2 shows the DTA records for the reference alloy and Figure 3 for the Sb-bearing alloy for the various cooling rates used in the present study. All curves show that the transformation takes place in two steps which appear better differentiated as the cooling rate is decreased. The thermal arrest at higher temperature relates to the development of ferrite, and the one at lower temperature to the formation of pearlite.[6] Using the time derivative of the signal, the experimental temperatures for the start of the ferritic reaction, $T_{\exp,\alpha}$, and for the start of the pearlitic reaction, $T_{\exp,p}$, could be estimated, they are plotted in Figure 4. As can be

observed, the temperatures for both the stable and metastable reactions appear slightly higher for the Sb-bearing alloy than for the reference alloy. This goes in line with the effect of antimony predicted by thermodynamic calculations as described in appendix, though here it may rather be due to the slight difference in silicon content between the two alloys. This will be discussed further later in this paper.

The first row in Figure 5 shows micrographs of a fully pearlitic and of a ferrito-pearlitic area of the Sb-bearing alloy and the second row is of the same areas after FIB. EDS mapping was performed in the rectangular zones marked on these latter micrographs. The signal of C, O, Mg, Al, Si, S, Ti, Cr, Mn, Fe, Ni, and Sb was mapped. It was observed that O and Mg are apparently present in higher amount in graphite than in the matrix, while this is the reverse for all the other elements. Furthermore, what is clear from these maps is that there is no build-up of any element at the interface between graphite and the matrix. This is illustrated by the example of the
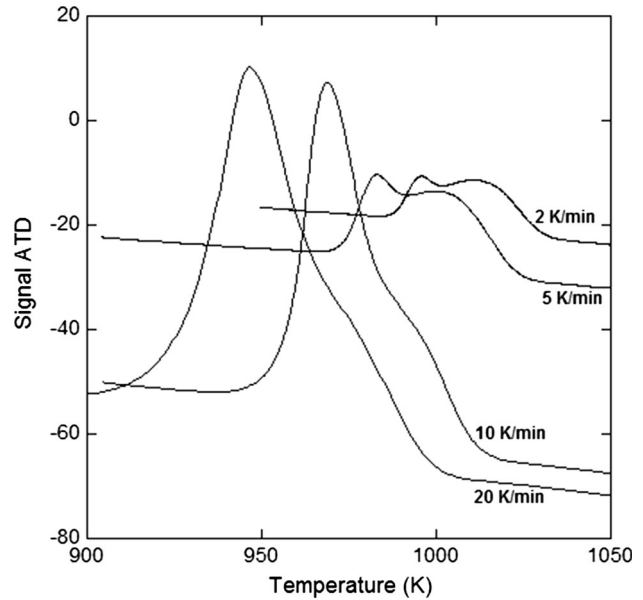
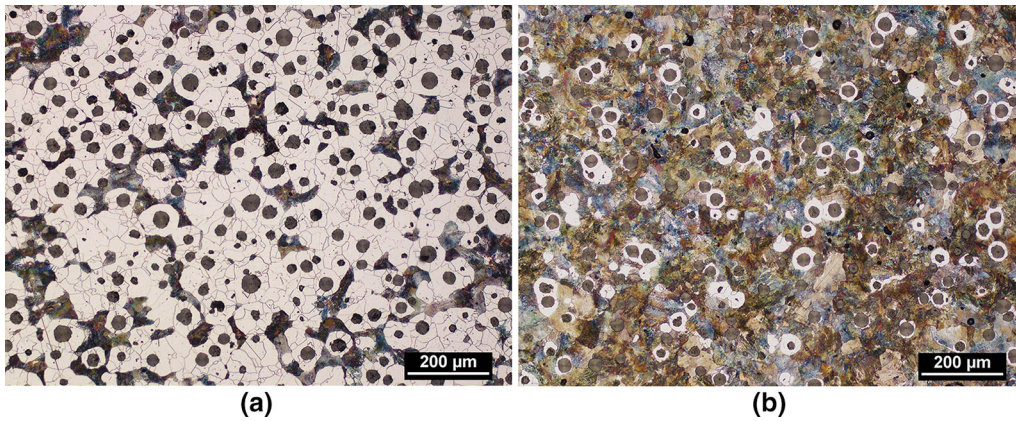

Fig. 2—DTA records for the reference alloy.

Fig. 1—OM micrograph of Nital etched as-cast samples of the reference alloy (*a*) and the Sb-bearing one (*b*).
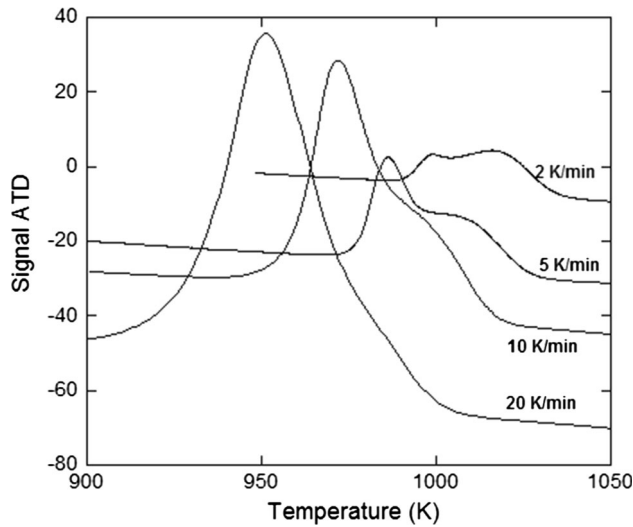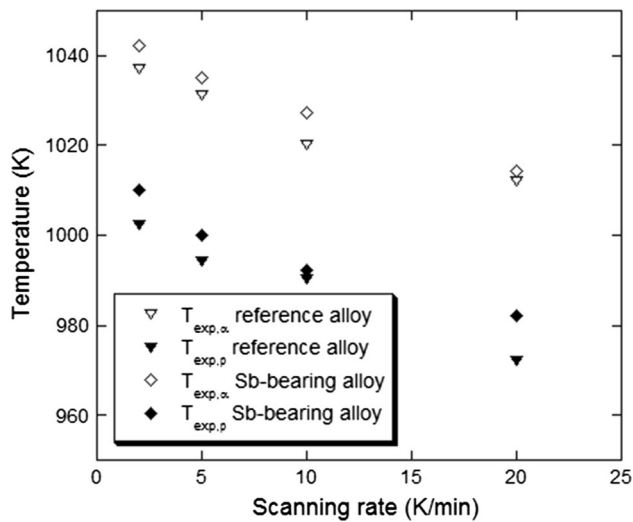
Fig. 3—DTA records for the Sb-bearing alloy.

Fig. 4—Effect of scanning rate on the temperatures for the start of the ferritic and pearlitic reactions as recorded by DTA.

antimony maps shown in the third row of Figure 5, though it is agreed that the signal was rather weak for this element (other maps are given as supplemental material).

While EDS mappings were only qualitative, microprobe measurements were fully quantitative though subject to scattering because of the nature of X-ray emission. In Table III are listed the maximum value of the detection limit and typical range (minimum and maximum) of the content for each measured element apart from silicon—the detection limit for silicon was 230 ppm and the measurements for this element were always far above this value. The maximum standard deviation σ was very similar to the detection limit for all elements. It was observed and it is seen in Table III that the reported contents in Al, Cu, Mg, and Sb could be zero. In most cases this related to saw-like line profiles when the local content in these elements was close to

their detection limit. Those elements that always gave satisfactory results are Cr, Mn, P, and Si.

In order to ascertain the appropriateness of the microprobe measurements for the present study, it seemed of interest to first consider lines going through fully ferritic areas. Two examples are illustrated in Figures 6 and 7 where the lines went all through between two neighboring nodules. In both figures, a quite smooth evolution is seen though some small-scale oscillations appear that are related to the normal variability of each measurement, being either positive or negative and scaling as $\pm\sigma$. The overall evolution shown by these traces is thus simply related to microsegregation developed during solidification. These traces however did certainly not go through last to solidify areas where microsegregations are expected to be more marked, see below.

In very few cases we were unlucky with measurement lines going either through unseen defects or through complex-shaped ferrite–pearlite boundaries. However, many lines crossing gently rounded ferrite/pearlite boundary could be safely analyzed. Figure 8(a) shows an OM micrograph of the as-cast reference sample where three lines of microprobe measurements can be seen, labeled 1, 2, and 3, which contain ferrite/pearlite boundaries. Looking at the sample at large enough enlargement, the measurement points may be distinguished as seen in Figure 8(b). In this case as in most cases, there was no need for etching the sample again after microprobe analysis to visualize the pearlitic areas as the final light polishing before microprobe measurements did not remove all the marking of previous etching.

The composition change along the microprobe line in Figure 8(b) is shown in Figure 8(c). This graph is of great interest as the area where pearlite appeared has about the same composition than the neighboring ferrite areas. Thus, in this case, this is only the slow kinetics of ferrite growth and the associated cooling of the material that may explain that pearlite appeared and grew at the expense of ferrite.

The micrograph in Figure 9(a) shows a microprobe line realized on the as-cast Sb-bearing alloy. This area should present boundaries between ferrite and pearlite which were confirmed by etching after microprobe analysis as shown in Figure 9(b). There, the transition from stable to metastable transformation has certainly been triggered by marked microsegregation of pearlite promoter elements (Cr, Mn,..). This figure shows much higher microsegregations than in the previous examples, and it may be guessed that the line went through a last to solidify area in this case.

The most important is that there is no indication of any composition change in substitutional solutes when crossing the ferrite/pearlite boundaries in Figures 8(c) and 9(c): the compositional field appears continuous and smoothly changing with distance to nodules. A check of all other microprobe Cr, Mn, P, and Si lines showed the same result, i.e., that no compositional step could be observed between ferrite and pearlite, but eventually smooth change could easily be associated with
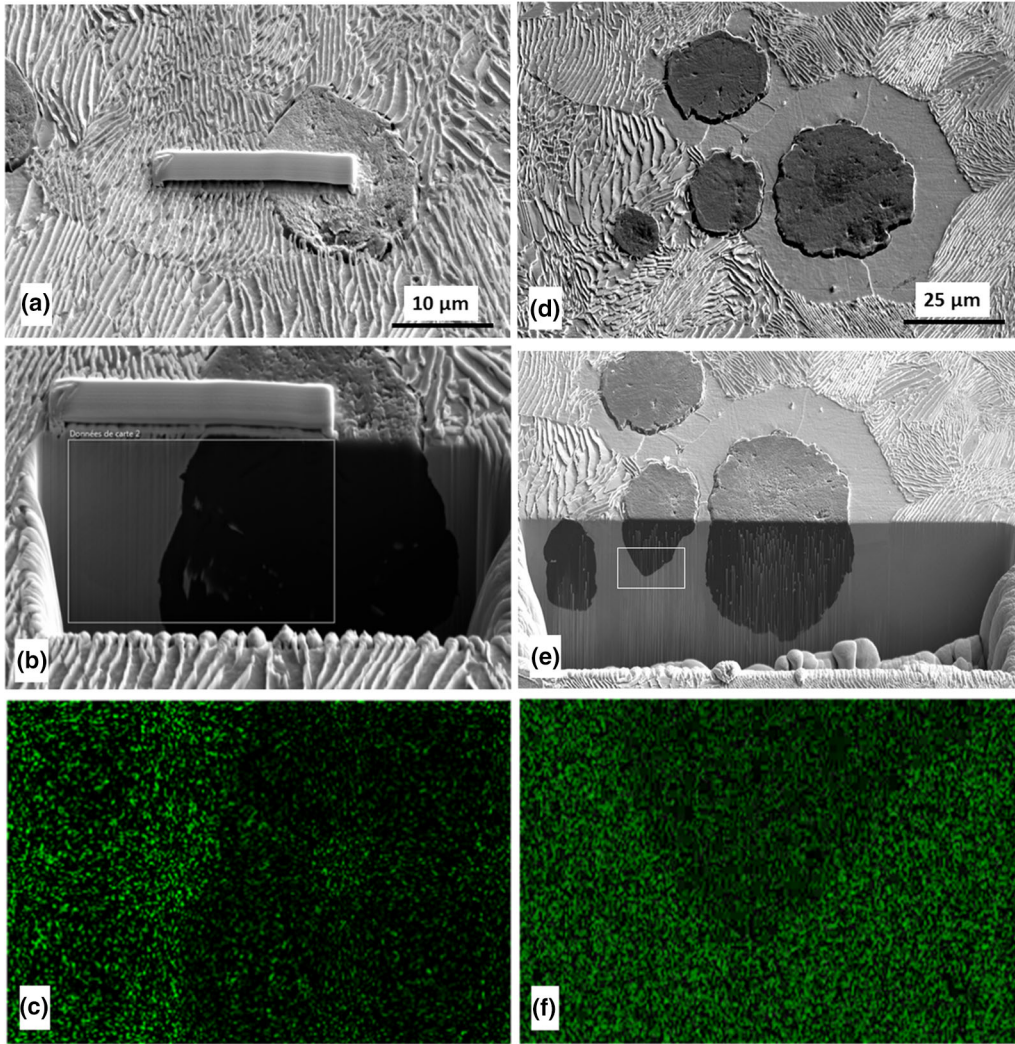
Fig. 5—SEM micrographs of two areas of the Sb-bearing alloy showing a fully pearlitic area (*a*, *b*, and *c*) and a ferritic–pearlitic one (*d*, *e*, and *f*) before drilling (first row) and after (second row). Maps of Sb distribution (third row) in the areas indicated as thin rectangles in the middle row images.

Table III. Maximum Value of the Microprobe Detection Limit for the Analyzed Elements, Standard Deviation of a Measurement, and Typical Minimum and Maximum Contents Recorded Along the Lines (ppm Per Mass)

Element	Al	Cr	Mg	P	Mn	Cu	Sb
Detection limit	220	140	290	190	530	1000	660
Minimum content	0	60	0	40	40	0	0
Maximum content	1500	1500	300	1500	3500	1200	250

solidification microsegregation as described by Boeri and Weinberg[7] among others.

Figure 10 compares the composition profiles in silicon, aluminum, and copper for the same line as in Figure 9(c). Though the distributions of aluminum and copper are seen to be parallel to that of silicon, it is observed how the statistical variation of the measurements for these elements gives a saw-like profile that made them of little use for the present study.

IV. DISCUSSION

As stressed previously,[4,8] the diffusion rate of substitutional solutes in austenite is so low that no long-range redistribution can take place during the eutectoid transformation under continuous cooling—for cooling rates higher than about 1.2 K/min.[9] This is very much as para-equilibrium described in steel transformation as described since the mid of the last century[10] and
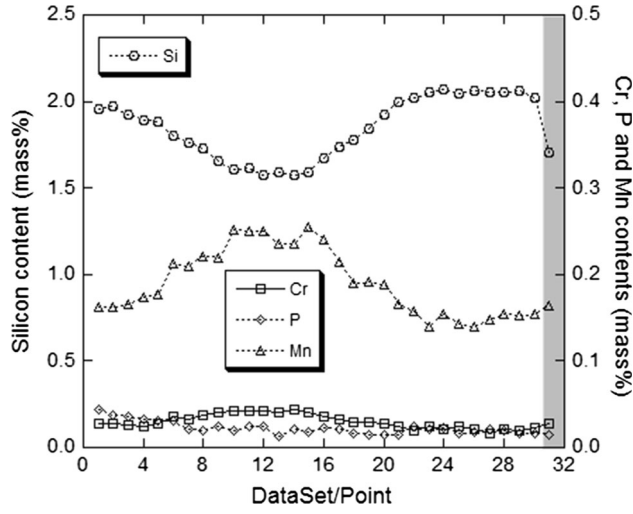
Fig. 6—Microprobe traces along a line joining two neighboring nodules, from the DTA short-cycle sample of the reference alloy. The matrix was fully ferritic in this area. The grayed area on the right corresponds to a measurement point located partly on the graphite nodule.
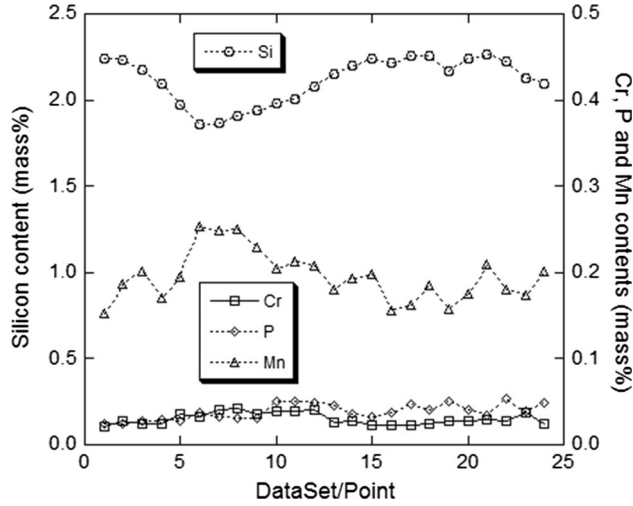

Fig. 7—Microprobe traces along a line joining two neighboring nodules, from the DTA long-cycle sample of the Sb-bearing alloy. The matrix was fully ferritic in this area.

was already considered by Venugopalan[11] in the case of cast irons though without experimental support. Accordingly, both the stable and metastable transformations proceed with the product—either ferrite or pearlite—inheriting the content in substitutional solutes of the parent austenite as observed with the present experimental results. The single reference found in the literature reporting compositional change between ferrite and austenite, ferrite and pearlite, and also pearlite and austenite is due to Guo and Stefanescu.[12] Though not giving much detail, the authors indicate that some eutectic carbides were present in the as-cast material they investigated which may better explain the abrupt

compositional changes they sometimes observed than the solid-state eutectoid transformations.

One further experimental proof that there is no composition change between parent austenite and either ferrite or pearlite is by looking at the correlation between the content in two elements. Figure 11 shows a plot of chromium and manganese contents *vs* silicon content for the short-cycle DTA sample of the reference alloy. The grayed rectangles in this figure represent the intrinsic variability of each measurement, the length of the horizontal side is $2 \cdot \sigma$ for silicon (about 0.05 mass pct) and that of the vertical side $2 \cdot \sigma$ for either chromium (about 0.03 mass pct) or manganese (about 0.1 mass pct). Similar plots that would exactly superimpose to this one were obtained for all five other samples. It is seen that the measurement points show a continuous evolution when separate clouds of points should have appeared if any abrupt compositional change had taken place during the eutectoid transformation.

If there is no compositional change between the parent austenite and either ferrite or pearlite, the eutectoid transformations can well be described in a Fe-C isopleth section of the relevant stable and metastable phase diagrams as those shown in appendix. It has been proposed that the upper temperature at which these transformations can proceed lies on the lower limit of the three-phase field.[4,8] These reference temperatures are denoted T_α in the stable system (Figure A1) and T_p in the metastable one (Figure A2). Using the thermodynamic calculations presented in appendix, the effect of antimony on the reference temperatures in the stable and metastable eutectoid reactions is estimated respectively to 7.1 and 6.1 K/mass pct. The relations linking the T_α and T_p reference temperatures (K) to composition have been previously estimated based on phase diagram calculations,[9] they are here complemented with the effect of antimony as:

$$
\begin{aligned}
T_\alpha = 273.15 + 739 + 18.4 w_{Si} + 2.0 (w_{Si})^2 \\
- 14.0 w_{Cu} - 45.0 w_{Mn} + 2.0 w_{Mo} \quad [1] \\
- 24.0 w_{Cr} - 27.5 w_{Ni} + 7.1 \cdot w_{Sb}
\end{aligned}
$$

$$
\begin{aligned}
T_p = 273.15 + 727 + 21.6 \cdot w_{Si} + 0.023 \cdot (w_{Si})^2 \\
- 21.0 \cdot w_{Cu} - 25.0 \cdot w_{Mn} + 8.0 \cdot w_{Mo} \quad [2] \\
+ 13.0 \cdot w_{Cr} - 33.0 \cdot w_{Ni} + 6.1 \cdot w_{Sb},
\end{aligned}
$$

where w_i is the mass pct content in i element in austenite.

Note that, for a given cast iron, the reference temperatures are to be calculated with the nominal element contents multiplied by about 1.05 to account for graphite precipitation assuming it is pure carbon.[4,8] For the reference and Sb-bearing alloys respectively, this leads to 1045.2 K and 1051.2 K (772.0 °C and 778.1 °C) for T_α and 1036.5 K and 1041.3 K (763.3 °C and 768.1 °C) for T_p. The differences between these temperatures are in excellent agreement with those seen in Figure 4. It should be stressed that the amount of antimony in both
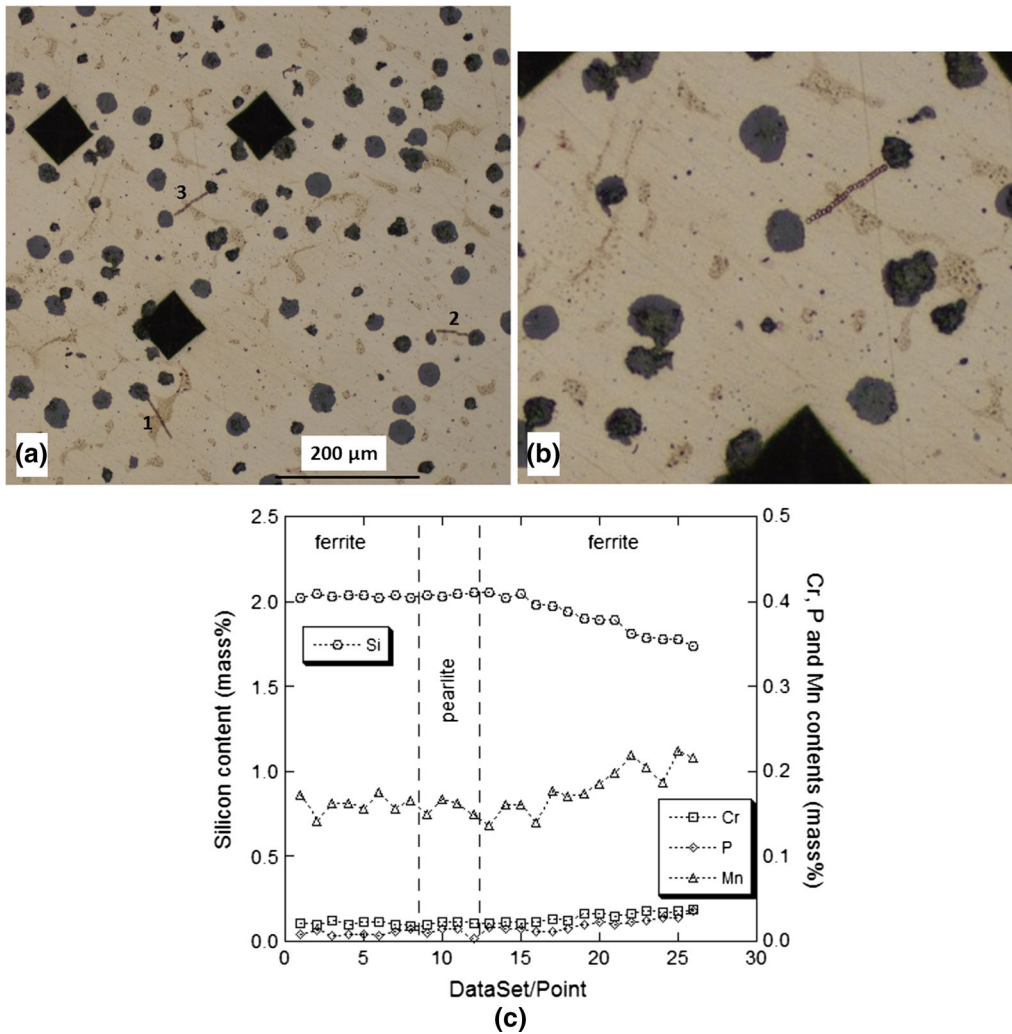
Fig. 8—(*a*) OM micrograph of the as-cast reference sample with visible lines of microprobe measurement points labeled 1, 2, and 3; (*b*) enlarged micrograph showing that individual measurement points can be identified along line #3; (*c*) microprobe trace along line #3 going from top-right to bottom-left.

alloys is by far too low to affect theses values, the difference here is due to the change in silicon content.

The undercooling for the start of the eutectoid transformations is thus expressed as $\Delta T_\alpha = T_\alpha - T_{exp,\alpha}$ for the ferritic reaction and $\Delta T_p = T_p - T_{exp,p}$ for the pearlitic reaction. The data in Figure 4 are plotted again as undercooling *vs* cooling rate in Figure 12. It is seen that the results for both alloys could be fitted with one single curve for each of the eutectoid reactions. The start of the ferritic reaction may be extrapolated to a zero undercooling at a zero cooling rate, while that for the pearlitic reaction would extrapolate to an undercooling of about 30 K. This shows that ferrite needs very low driving force for nucleation while nucleation of cementite for the pearlitic reaction to proceed requires a significant driving force. This agrees with previous results on ferrito-pearlitic irons with less than about

0.05 mass pct tin.[5,8,13] However, it was observed that at tin levels higher than 0.05 mass pct the undercooling for the start of the pearlitic reaction decreased dramatically, and in fact could be extrapolated to a zero undercooling at a zero cooling rate.[5] This would mean that at such a level, tin triggers nucleation of cementite and thus of pearlite. It would be of great interest in investigating if antimony leads to the same results above some critical limit to be determined.

At low level as in the present study, antimony appears to affect the eutectoid reaction as tin does, in that it increases effectively the amount of pearlite without decreasing significantly the undercooling for the pearlitic reaction. This suggests that antimony decreases the rate of ferrite growth, and this must be by adsorbing at the graphite surface and diminishing the possibility for carbon atoms to precipitate on graphite. Such an
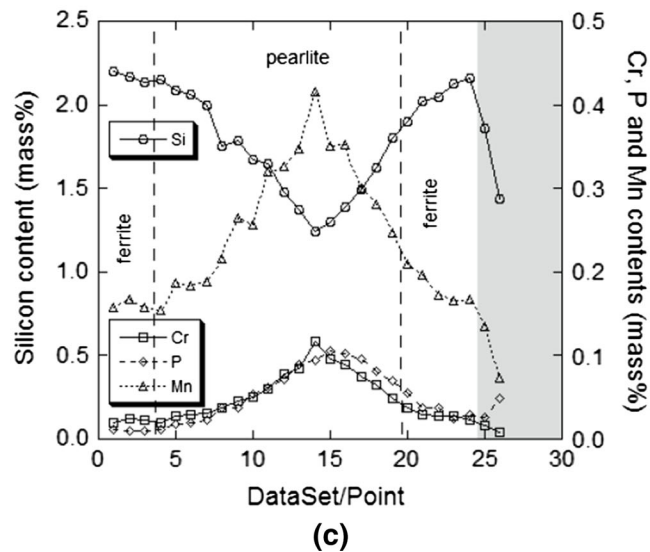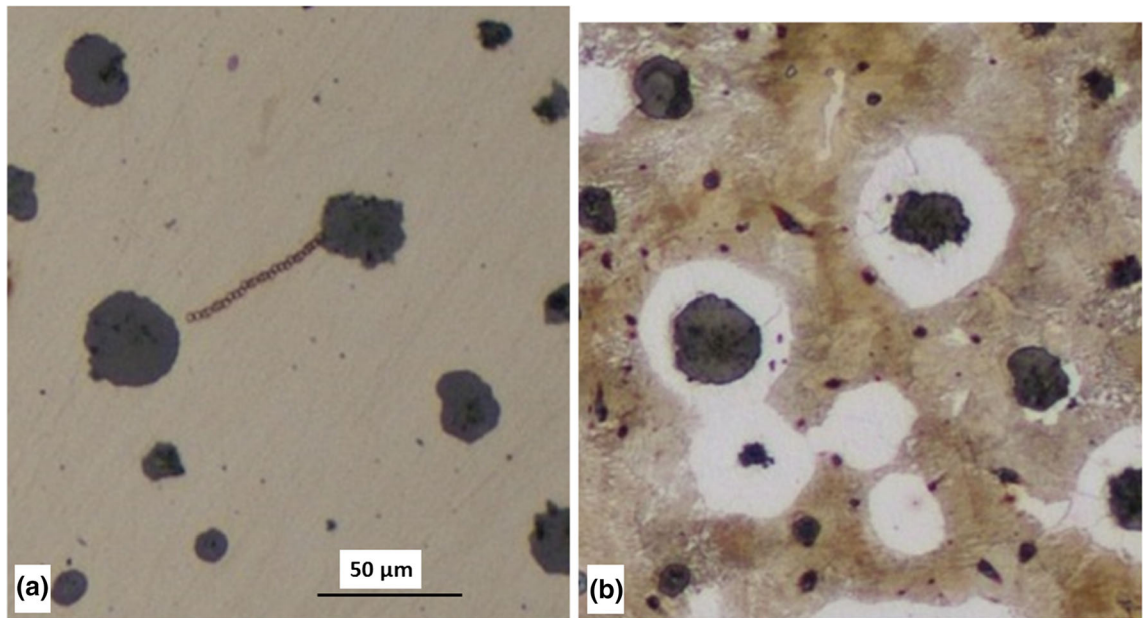
Fig. 9—(a) OM micrograph of the as-cast Sb-bearing sample with visible line of microprobe measurement points; (b) view of the same zone after etching; (c) microprobe trace along a line joining two neighboring nodules, carried out from bottom-left to top-right. The grayed area on the right corresponds to two measurement points located on the graphite nodule.

adsorption has not been seen in the present FIB analysis but it has been reported by Johnson and Kovacs[14] on alloys containing higher additions at 0.07 mass pct Sb and 0.11 mass pct Sn. Interestingly enough, Bofan and Langer[15] observed antimony accumulated in graphite lamellas as compared to the matrix in an alloy containing 0.25 mass pct Sb, while Kovacs[16] could not find an adsorption layer in lamellar irons with up to 0.055 mass pct Sb and up to 0.061 mass pct Sn while these elements are also pearlite promoters for these alloys. These contradictions stress the interest of performing more work in this area. Secondary ion mass spectroscopy (SIMS) is expected to give better results for such a goal than EDS or Auger analyses which have a detection limit of at best 0.2 to 0.3 mass pct for the most usual alloying elements in cast irons even when quantitative analysis is looked for.

The present results illustrated also the interplay between cooling rate and microsegregation issued from the solidification step. In the last to solidify areas, these microsegregations strongly favor the formation of pearlite because of the decrease in the silicon content and the increase in, e.g., the manganese and chromium contents. However, it has been shown that in common cast irons microsegregations affect the local reference temperatures only in the part of the alloy that relates to the last 20 pct to solidify.[17] Accordingly, the start temperatures for the stable and metastable eutectoid transformations as reported here
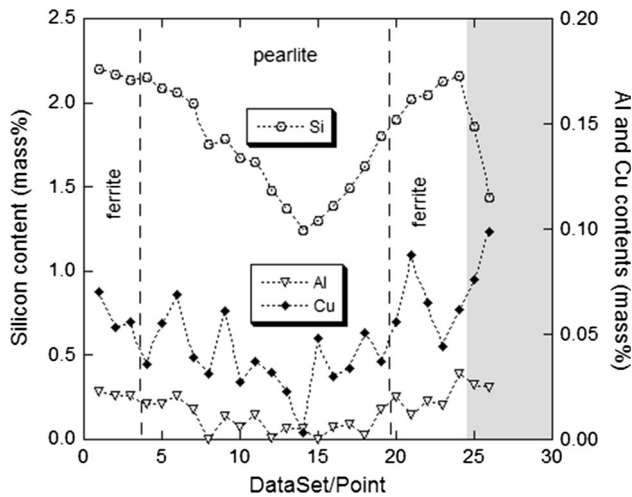
Fig. 10—Microprobe traces along a line joining two neighboring nodules, from the as-cast Sb-bearing sample. This is in the same line as in Fig. 9 but with here the contents in aluminum, copper, and silicon.
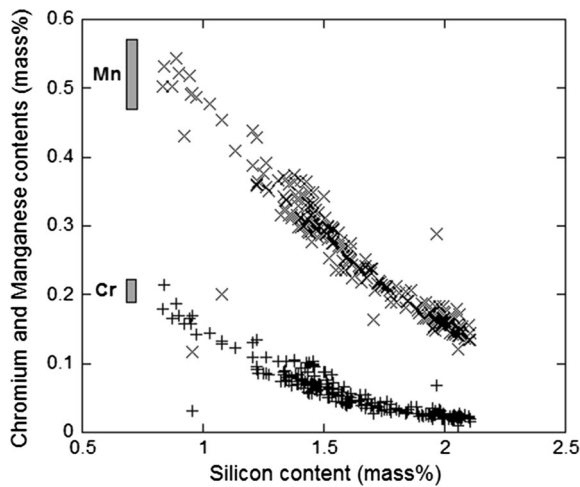

Fig. 11—Correlation between individual measurements in silicon *vs* chromium and manganese contents. The rectangles represent the intrinsic variability of each measurement, the length of the horizontal side is $2\cdot\sigma$ for silicon (about 0.05 mass pct) and that of the vertical side $2\cdot\sigma$ for either chromium (about 0.03 mass pct) or manganese (about 0.1 mass pct).

should not be much affected by microsegregation issued from the solidification step.

V. CONCLUSION

The present results showed that antimony acts as tin at low-level addition in significantly increasing the amount of pearlite in nodular cast iron without significantly changing the transformation temperatures and undercoolings. It would be of great interest to complement the present work on alloys with higher antimony levels for investigating if there is a critical amount over
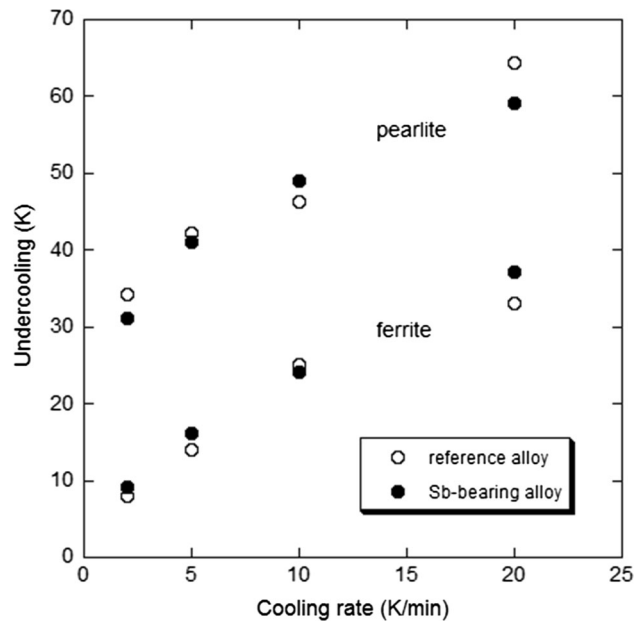

Fig. 12—Evolution with the cooling rate of the undercooling for the start of the ferritic and pearlitic reactions.

which undercooling for the start of the pearlitic reaction decreases as this is the case for tin.

The present work demonstrates also that composition profiles across ferrite/pearlite boundaries are smooth and similar to those issued from the solidification step. No trace of long-range diffusion of substitutional solutes could be detected which goes in line with the statement that, under continuous cooling at a rate higher than 1.2 K/min, both stable and metastable transformations proceed with the product matrix—either ferrite or pearlite—inheriting the parent austenite content in substitutional solutes. This is in line with the so-called local para-equilibrium model which is commonly used for describing solid-state eutectoid transformation in steels. The lack of prior similar reports for cast irons in literature may be due to the fact that showing smooth composition profiles must have been considered as not being worthy of publication.

APPENDIX

The thermodynamic evaluation of the Fe-Sb phase diagram by Benyan Pei *et al.*[18] has been introduced in the available SSOL databank that was last updated in 1998. The only change made to this latter bank is the improvement of the Fe-C-Si system performed by Miettinen[19] to the earlier assessment by Lacaze and Sundman.[20] Owing to the very limited amount of antimony relevant for cast irons production (0.1 mass pct at most), it could be considered that appropriate calculations for Fe-C-Si-Sb alloys could be performed without further modifications. Figures A1 and A2 compare isopleth Fe-C sections of, respectively, the stable and metastable systems at 2.0 mass pct Si and 0
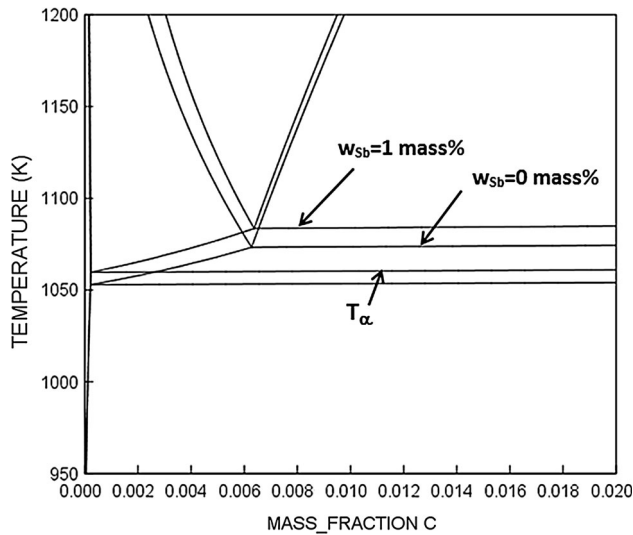
Fig. A1—Isopleth Fe-C section of the stable Fe-C-Si-Sb phase diagram at 2.0 mass pct Si and 0 and 1 mass pct Sb in the temperature range of the eutectoid transformation. The T_α reference temperature for the alloy at 1 mass pct Sb is indicated with an arrow.
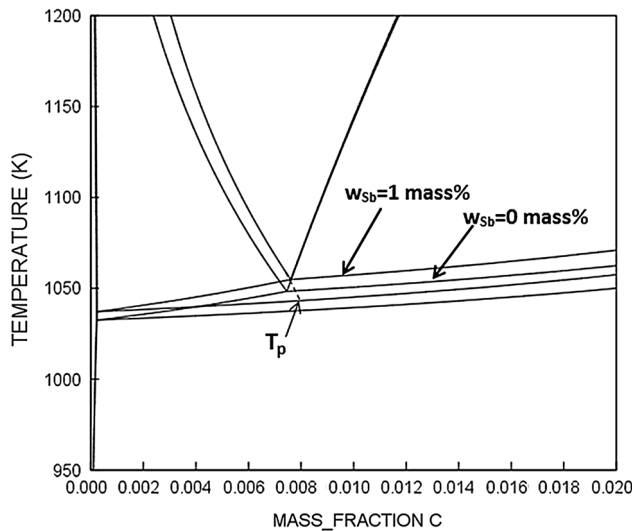

Fig. A2—Isopleth Fe-C section of the metastable Fe-C-Si-Sb phase diagram at 2.0 mass pct Si and 0 and 1 mass pct Sb in the temperature range of the eutectoid transformation. The T_p reference temperature is assumed to be on the extrapolation of the γ/α equilibrium line as indicated with an arrow for the alloy at 1 mass pct Sb.

and 1 mass pct Sb. According to these figures, 1 mass pct antimony shifts slightly both the stable and metastable eutectoid ranges to higher temperature. The T_α and T_p reference temperatures used in the main text are shown in Figures A1 and A2, respectively.

ELECTRONIC SUPPLEMENTARY MATERIAL

The online version of this article (doi:10.1007/s11661-016-3692-3) contains supplementary material, which is available to authorized users.

REFERENCES

1. E. Dorazil: *High Strength Austempered Ductile Cast Iron*, Ellis Horwood Ltd. and Academia, Praha, 1991, pp. 13–23.
2. J.M. Schissler: Hommes et Fonderie, 1986, pp. 13–23.
3. K.B. Rundman: Proc. of 101 Casting Congress, 1997, AFS, paper 97-117.
4. J. Lacaze: ASM Handbook, Cast Irons, vol. 1A, 2016 (to appear).
5. J. Lacaze and J. Sertucha: *Inter. J. Cast Met. Res.*, 2016, vol. 29, pp. 74–78.
6. U. Ekpoom and R.W. Heine: *AFS Trans.*, 1978, vol. 86, pp. 281–86.
7. R. Boeri and F. Weinberg: *Cast Met.*, 1993, vol. 6, pp. 153–58.
8. J. Lacaze, C. Wilson, and C. Bak: *Scand. J. Metall.*, 1994, vol. 23, pp. 151–63.
9. V. Gerval and J. Lacaze: *ISIJ Int.*, 2000, vol. 40, pp. 386–92.
10. A. Hultgren: *Trans. ASM*, 1947, vol. 39, pp. 915–1005.
11. D. Venugopalan: *Proceedings of the International Symposium on Fundamentals and applications of ternary diffusion*, G.R. Purdy, ed., Hamilton, Canada, 1990, pp. 173–83.
12. X. Guo and D.M. Stefanescu: *IJCMR*, 1999, vol. 11, pp. 437–41.
13. J. Lacaze, A. Boudot, V. Gerval, D. Oquab, and H. Santos: *Metall. Mater. Trans.*, 1997, vol. 28A, pp. 2015–25.
14. W.C. Johnson and B.V. Kovacs: *Metall. Trans. A*, 1978, vol. 9, pp. 219–29.
15. Z. Bofan and E.W. Langer: *Scand. J. Metall.*, 1984, vol. 13, pp. 23–31.
16. B.V. Kovacs: *AFS Trans.*, 1980, vol. 89, pp. 79–96.
17. V. Gerval and J. Lacaze: *Proceedings of SP97, 4th Decennial International Conference on Solidification Processing*, eds J. Beech and H. Jones, University of Sheffield, 1997, pp. 506–10.
18. B. Pei, B. Björkman, B. Sundman, and B. Jansson: *CALPHAD*, 1995, vol. 19, pp. 1–15.
19. J. Miettinen: *CALPHAD*, 1998, vol. 22, pp. 231–56.
20. J. Lacaze and B. Sundman: *Metall. Trans. A*, 1991, vol. 22A, pp. 2211–23.